Variations in initial ^{26}Al/^{27}Al ratios among fine-grained Ca-Al-rich inclusions from reduced CV chondrites

Noriyuki Kawasaki [a,*], Sohei Wada [a], Changkun Park [b], Naoya Sakamoto [c], Hisayoshi Yurimoto [a,c,d]

[a] *Department of Natural History Sciences, Hokkaido University, Sapporo 060-0810, Japan*
[b] *Division of Earth-System Sciences, Korea Polar Research Institute, Incheon 21990, Republic of Korea*
[c] *Isotope Imaging Laboratory, Creative Research Institution, Hokkaido University, Sapporo 001-0021, Japan*
[d] *Institute of Space and Astronautical Science, Japan Aerospace Exploration Agency, Sagamihara 252-5210, Japan*

Abstract

Fine-grained Ca-Al-rich inclusions (FGIs) in CV chondrites are suggested to be condensates formed directly from the solar nebular gas. Al–Mg mineral isochrons of seven FGIs from reduced CV chondrites Efremovka, Vigarano, Thiel Mountains 07007, and Northwest Africa 8613 were obtained via *in situ* Al–Mg isotope measurements using secondary ion mass spectrometry. The slopes of the mineral isochrons for seven FGIs exhibit statistically significant variations in initial ^{26}Al/^{27}Al ratios, $(^{26}$Al/^{27}Al$)_0$, ranging from (5.19 ± 0.17) to $(3.35 \pm 0.21) \times 10^{-5}$, which correspond to a relative age spread of 0.44 ± 0.07 Myr. Inferred upper limit of $(^{26}$Al/^{27}Al$)_0$ for the FGIs is identical to the Solar System $(^{26}$Al/^{27}Al$)_0$ of $\sim5.2 \times 10^{-5}$ as determined by whole-rock Al–Mg isochron studies for CAIs in CV chondrites. The intercepts of the mineral isochrons, the initial ^{26}Mg/^{24}Mg ratios the FGIs formed with, are consistent with Mg-isotope evolution path of a solar-composition nebular gas. The observed variations in $(^{26}$Al/^{27}Al$)_0$ for FGIs are essentially similar to those (~5.2 to $\sim4.2 \times 10^{-5}$) for coarse-grained, igneous CAIs of CV chondrites that are formed by melting and solidification. If ^{26}Al was distributed homogeneously in the forming region, then our data indicate that thermal processes of condensation and melting for CAI formation occurred contemporaneously and continued for at least ~0.4 Myr at the very beginning of the Solar System. Alternatively, the observed variations in $(^{26}$Al/^{27}Al$)_0$ also indicate the possibility of heterogeneous distributions of ^{26}Al in the forming region, corresponding to a range of over at least $3.4 \times 10^{-5} < (^{26}$Al/^{27}Al$)_0 < 5.2 \times 10^{-5}$.
© 2020 Elsevier Ltd. All rights reserved.

1. INTRODUCTION

Ca-Al-rich inclusions (CAIs) in chondrites are the oldest objects formed in our Solar System with an average age of 4567.30 ± 0.16 Ma as determined by U-corrected Pb–Pb absolute chronology (Connelly et al., 2012). CAIs had incorporated live-^{26}Al, a short-lived radionuclide with a half-life of 0.705 Myr (Norris et al., 1983), at the time of their formation (e.g., Lee et al., 1976; MacPherson et al., 1995). The initial ^{26}Al abundances for CAIs and other various Solar System materials can be applied to infer relative chronology of the early Solar System (e.g., Kita et al., 2013). Several studies suggested that ^{26}Al was homogeneously distributed throughout at least the region of the Solar System where "canonical" CAIs in CV chondrites formed (e.g., MacPherson et al., 1995; Jacobsen et al., 2008; Larsen et al., 2011). Conversely, heterogeneous

* Corresponding author.
E-mail address: kawasaki@ep.sci.hokudai.ac.jp (N. Kawasaki).

distributions of ^{26}Al in the inner solar protoplanetary disk have also been suggested from multiple meteoritic records, (1) presence of ^{26}Al-poor refractory objects, such as FUN CAIs in CV chondrites (e.g., Wasserburg et al., 1977; Park et al., 2017 and references therein), corundum grains in carbonaceous and unequilibrated ordinary chondrites (Makide et al., 2011), grossite- and hibonite-rich CAIs in CH and CH/CB chondrites (e.g., Krot et al., 2008), and hibonite-rich CAIs with large nucleosynthetic anomalies of Ti and Ca isotopes in CM chondrites (e.g., Kööp et al., 2016 and references therein), (2) Al–Mg isotopic compositions of bulk chondrites (Larsen et al., 2011), and (3) age mismatches between U-corrected Pb–Pb and ^{26}Al–^{26}Mg systems for angrites (Schiller et al., 2015) and individual chondrules (Bollard et al., 2019).

CAIs are considered to have experienced complex thermal histories in the solar nebular gas having variable isotope compositions during the formation (e.g., Yurimoto et al., 2008; MacPherson, 2014; Krot, 2019 and references therein). Coarse-grained, igneous CAIs in CV chondrites, such as compact Type A, Type B, and Type C CAIs, experienced melting of precursor solids and crystallization from a melt (e.g., MacPherson and Grossman, 1981; Wark and Lovering, 1982; Wark, 1987; Yurimoto et al., 1998). High-precision Al–Mg mineral isochron studies using secondary ion mass spectrometry (SIMS) revealed that initial ^{26}Al/^{27}Al ratios, $(^{26}Al/^{27}Al)_0$, for compact Type A and Type B CAIs in CV chondrites range from ∼5.2 to ∼4.2 × 10^{-5}, which correspond to a relative formation age spread of ∼0.2–0.3 Myr (Kita et al., 2012; MacPherson et al., 2012, 2017, 2018; Kawasaki et al., 2018). Formation events of Type C CAIs are likely related to the chondrule formation and they exhibit significantly lower $(^{26}Al/^{27}Al)_0$ for their last melting events, corresponding to a relative age of >∼2 Myr after formation of most CAIs (e.g., Krot et al., 2005, 2007; Kawasaki et al., 2015).

Coarse-grained, fluffy Type A (FTA) CAIs of CV chondrites generally exhibit irregular shapes with aggregate structures and are composed mainly of gehlenitic melilite (MacPherson and Grossman, 1984; Katayama et al., 2012; Kawasaki et al., 2012). They do not display signatures of later extensive melting and can be formed by gas–solid condensation (MacPherson and Grossman, 1984; Katayama et al., 2012; Kawasaki et al., 2017). There are three FTA CAIs obtained for high-precision Al–Mg mineral isochrons and they show $(^{26}Al/^{27}Al)_0$ ranging from ∼5.1 to ∼4.4 × 10^{-5} (MacPherson et al., 2012; Kawasaki et al., 2017, 2019), which is similar to those for the igneous CAIs and corresponds to a relative formation age spread of ∼0.2 Myr.

Spinel-rich, fine-grained inclusions (FGIs) in CV chondrites are suggested as condensates directly from the solar nebular gas, based on their volatility-fractionated trace-element patterns (Boynton, 1975; Davis and Grossman 1979) and complex multi-layered structures (Wark and Lovering, 1977; Krot et al., 2004a). Two spinel-rich FGIs in CV chondrites are examined for high-precision Al–Mg mineral isochron and they exhibit apparently constant $(^{26}Al/^{27}Al)_0$ of ∼5.2 × 10^{-5} (MacPherson et al., 2010; Kawasaki et al., 2019), being identical to the whole-rock

CAI $(^{26}Al/^{27}Al)_0$ (Jacobsen et al., 2008; Larsen et al., 2011). Given the limited number for Al–Mg data of FGIs, relationships of $(^{26}Al/^{27}Al)_0$ between igneous CAIs and condensate CAIs are still poorly understood although this type of an investigation enables constraining chronological relationships between high-temperature thermal processes of condensation and melting of CAI minerals in the earliest Solar System.

FGIs in the reduced CV chondrites preserve the original mineral assemblages formed by condensation, which consist mainly of spinel, melilite, anorthite, and aluminous diopside with more rarely perovskite and hibonite (Krot et al., 2004a), however, in FGIs from oxidized CV chondrites, such as Allende, original anorthite and melilite have been replaced by secondary minerals such as nepheline and sodalite (MacPherson, 2014). In this study, we present Al–Mg mineral isochrons for seven FGIs from reduced CV chondrites, Efremovka, Vigarano, Thiel Mountains (TIL) 07007, and Northwest Africa (NWA) 8613 via in situ isotope analysis with SIMS. The isochrons enable (1) a more systematic comparison of $(^{26}Al/^{27}Al)_0$ between igneous CAIs and condensate CAIs than that achieved in previous studies and (2) quantitative investigations of Mg-isotope evolution of FGIs to provide constraints on a gaseous reservoir from which they condensed.

2. EXPERIMENTAL TECHNIQUES

2.1. Sample preparation and elemental analysis

FGIs *HKE02* and *HKE03* are included in a polished section of Efremovka (Fig. 1), which also includes an FTA CAI *HKE01* (Kawasaki et al., 2012, 2019). An FGI *HKV03* is found in a polished section of Vigarano. FGIs *TIL01*, *TIL02*, and *TIL03* are found in a polished thin section of TIL 07007. An FGI *HKD01* is found in a polished section of NWA 8613. The polished sections were coated with a carbon thin film (∼20 nm) for backscattered electron (BSE) imaging, elemental analysis using an energy dispersive X-ray spectrometer (EDS), and electron backscatter diffraction (EBSD) mapping. Subsequently, they were coated with a gold thin film (∼70 nm) for in situ Al–Mg isotope measurements using SIMS.

BSE images were obtained via a field emission type scanning electron microscope (FE-SEM; JEOL JSM-7000F) at Hokkaido University. Quantitative elemental analysis and X-ray elemental mapping were conducted via an energy dispersive X-ray spectrometer (EDS; Oxford X-Max 150) installed on the FE-SEM. A 15 keV electron beam probe with currents of 1 nA (for quantitative analysis) and 10 nA (for mapping) was employed in the present study. Bulk Al/Mg chemical compositions of FGIs were estimated as an average of multiple measurements covering the entire CAIs via a raster electron beam. We calculated ^{27}Al/^{24}Mg ratios for each FGI from the bulk Al/Mg chemical compositions obtained by EDS assuming terrestrial reference ratios of ^{25}Mg/^{24}Mg = 0.12663 and ^{26}Mg/^{24}Mg = 0.13932 (Catanzaro et al., 1966). Crystal orientation mapping of the CAI minerals was performed via an EBSD system (AZtec HKL) equipped with the FE-SEM with a 20 keV
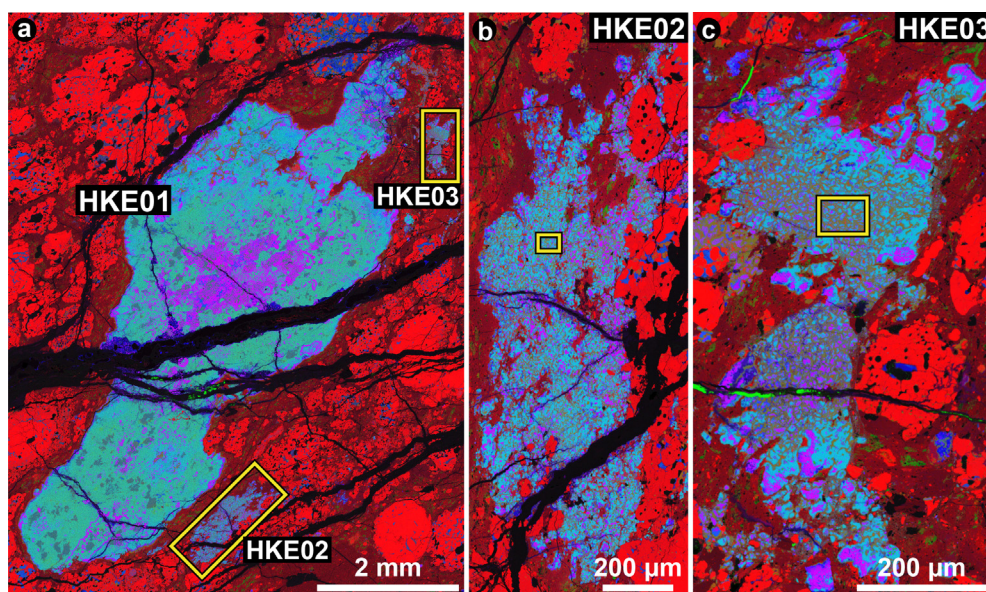
Fig. 1. Combined X-ray elemental map of (a) fluffy Type A CAI *HKE01*, (b) fine-grained CAI *HKE02* and (c) fine-grained CAI *HKE03* from Efremovka. Mg is denoted in red, Ca is denoted in green, and Al is denoted in blue. The yellow boxes in (a) indicate the areas shown in (b) and (c). The yellow box in (b) indicates the area shown in Fig. 2a and b. The yellow box in (c) indicates the area shown in Fig. 2c and d. Corresponding back scattered electron images are shown in Fig. S1.

electron beam probe and a current of 4 nA to determine grain boundaries of each crystalline mineral. Qualitative X-ray elemental mapping was simultaneously performed with EBSD crystal orientation mapping.

2.2. Al–Mg isotope analysis in multicollection mode

Mg-isotopes and $^{27}Al/^{24}Mg$ ratios of minerals in the FGIs were measured via the SIMS instrument (Cameca ims-1280HR) at Hokkaido University. An $^{16}O^-$ primary beam accelerated to 23 keV was employed in the experiment. We used the peak-jumping mode and multicollection mode based on the secondary ion intensities of Mg-isotopes from the minerals. For the analysis of spinel and olivine, the Mg-isotopes ($^{24}Mg^+$, $^{25}Mg^+$, and $^{26}Mg^+$) and $^{27}Al^+$ were simultaneously measured in multicollection mode with four Faraday cups: $^{24}Mg^+$ for L2* (10^{11} Ω), $^{25}Mg^+$ for L1 (10^{11} Ω), $^{26}Mg^+$ for H1 (10^{11} Ω), and $^{27}Al^+$ for H2* (10^{10} Ω or 10^{11} Ω). The primary beam current was set to 0.9–4.6 nA with an elliptical shape of 5×8 to 8×13 μm for spinel measurements and a 2.5 nA beam with an elliptical shape of 6×10 μm was used for olivine measurements. The beam sizes are comparable to or may slightly exceed crystal sizes of objective minerals in FGIs although all the measurements confirmed that the sputtered craters are perfectly monomineralic. The mass resolution of $M/\Delta M$ was set at ~2000. The contributions of ion interferences (e.g., $^{24}MgH^+$, $^{25}MgH^+$, and $^{52}Cr^{2+}$) were negligible under these conditions. The secondary ion intensities of $^{24}Mg^+$ were approximately 0.5–1.8 × 10^8 and 2.4 × 10^8 cps for spinel and olivine, respectively. Each measurement was conducted for 20–40 cycles having a counting time of 10 s. The obtained count rates were corrected for FC background and relative yield of each detector. The relative sensitivity

factors for aluminum and magnesium were determined via measurements of Russian spinel and San Carlos olivine for spinel and olivine, respectively. The $\delta^{25}Mg$ values of spinel and olivine in FGIs were calculated after corrections of instrumental mass fractionation by assuming that $\delta^{25}Mg$ of the Russian spinel and San Carlos olivine are zero.

The excess of radiogenic ^{26}Mg, $\delta^{26}Mg^*$, was calculated via an exponential fractionation law with coefficient $\alpha_{natural} = 0.5128$ because natural fractionation for Mg-isotopes is considered to be controlled by evaporation processes (Davis et al., 2015). However, the natural mass fractionation deviates from the instrumental mass fractionation of SIMS, and the instrumental mass fractionation also differs among target minerals and among analytical sessions under the measurement conditions (Itoh et al., 2008; Kawasaki et al., 2017, 2018, 2019). We determined instrumental mass fractionation, α_{SIMS}, via measurements of terrestrial standards to calculate the excess radiogenic ^{26}Mg in each analytical session. The α_{SIMS} value for spinel was determined via linear regression of the $\Phi^{25}Mg$ and $\Phi^{26}Mg$ values of Takashima augite and Russian spinel, while the α_{SIMS} value for olivine was determined via linear regressions of the $\Phi^{25}Mg$ and $\Phi^{26}Mg$ values of Takashima augite and San Carlos olivine, where $\Phi^{25,26}Mg = 1000 \times \ln [(^{25,26}Mg/^{24}Mg)_{sample}/(^{25,26}Mg/^{24}Mg)_{ref.}]$. The terrestrial reference ratios of $(^{25}Mg/^{24}Mg)_{ref.} = 0.12663$ and $(^{26}Mg/^{24}Mg)_{ref.} = 0.13932$ (Catanzaro et al., 1966) were used for $\delta^{26}Mg^*$ calculations, although the final corrected-$\delta^{26}Mg^*$ values are independent of the ratios taken from reference. In this study, the α_{SIMS} for spinel was found to be 0.525 ± 0.004, 0.480 ± 0.004, 0.512 ± 0.004, 0.501 ± 0.005, and 0.515 ± 0.004 for different five sessions, and the α_{SIMS} for olivine was 0.523 ± 0.005 (2σ). From the results of the linear regressions, an instrumental offset for the

δ^{26}Mg* values, β, which ranged from -0.43 to -0.93 with 2σ errors of 0.01–0.02 depending on minerals and analytical sessions, was identified. The fractionation corrected-δ^{26}Mg* values for CAI minerals were determined by the following equation

$$\delta^{26}\text{Mg}* = \delta^{26}\text{Mg}_{\text{sample}} - \left[\left(1 + \frac{\delta^{25}\text{Mg}_{\text{sample}}}{1000} \right)^{\frac{1}{\alpha_{\text{natural}}}} - 1 \right]$$
$$\times 1000 - \beta + \left[\left(1 + \frac{\delta^{25}\text{Mg}_{\text{std}}}{1000} \right)^{\frac{1}{\alpha_{\text{natural}}}} - 1 \right] \times 1000$$
$$- \left[\left(1 + \frac{\delta^{25}\text{Mg}_{\text{std}}}{1000} \right)^{\frac{1}{\alpha_{\text{SIMS}}}} - 1 \right] \times 1000,$$

where $\delta^{25,26}$Mg$_{\text{sample}} = [(^{25,26}\text{Mg}/^{24}\text{Mg})_{\text{sample}}/(^{25,26}\text{Mg}/^{24}\text{Mg})_{\text{ref.}} - 1] \times 1000$, δ^{25}Mg$_{\text{std}} = [(^{25}\text{Mg}/^{24}\text{Mg})_{\text{std}}/(^{25}\text{Mg}/^{24}\text{Mg})_{\text{ref.}} - 1] \times 1000$. More details and our error estimation procedure are described elsewhere (Kawasaki et al., 2017). The analytical errors (2σ) for δ^{26}Mg* were 0.09–0.10‰ for olivine and 0.09–0.18‰ for spinel.

2.3. Al–Mg isotope analysis in peak-jumping mode

For melilite and anorthite, Mg-isotopes (^{24}Mg$^+$, ^{25}Mg$^+$, and ^{26}Mg$^+$) were measured using an axial electron multiplier, while ^{27}Al$^+$ was measured using a multicollector Faraday cup (10^{11} Ω, designed for H2*) simultaneously with ^{25}Mg$^+$, in peak-jumping mode. An ^{16}O$^-$ primary beam accelerated to 23 keV was employed in the experiment. The primary beam current was set to 130–140 pA with a beam size of 4–7 μm for melilite measurements and a ~180 pA beam with a beam size of ~5 μm was used for anorthite measurements. The beam sizes are comparable to or may be slightly larger than crystal sizes of objective minerals in FGIs although all the measurements confirmed that the sputtered craters are perfectly monomineralic. The mass resolution of $M/\Delta M$ was set at ~4000, which is sufficient to resolve ion interferences (e.g., ^{48}Ca^{2+}, ^{24}MgH$^+$, ^{25}MgH$^+$, and ^{52}Cr^{2+}). The secondary ion intensities of ^{24}Mg$^+$ were 0.1–1.5 × 10^5 and 2–7 × 10^3 cps for melilite and anorthite, respectively. Each measurement was conducted for 100 cycles with a counting sequence with ^{24}Mg$^+$ for 2 s, ^{25}Mg$^+$ for 2 s, ^{25}Mg$^+$ and ^{27}Al$^+$ for 4 s, and ^{26}Mg$^+$ for 6 s. The obtained count rates were corrected for the FC background and EM deadtime. The instrumental mass fractionation and relative sensitivity factors for aluminum and magnesium were determined via measurements of synthetic melilite glasses (^{27}Al/^{24}Mg = 96 and 39) and synthetic anorthite glass (^{27}Al/^{24}Mg = 330) for melilite and anorthite, respectively. Details of synthetic glasses and relative sensitivity factors are described partly elsewhere (Kawasaki et al., 2019). The calculation method of δ^{26}Mg* is essentially identical to those described in Section 2.3 although α_{SIMS} and β were not determined in the peak-jumping mode because the instrumental mass fractionation and natural mass fractionation were indistinguishable from each other under the measurement conditions here. The analytical errors for δ^{26}Mg* were

assigned as internal errors (2SE) and were 1.1–3.8‰ and 4.7–10.3‰ for melilite and anorthite, respectively.

3. RESULTS

3.1. Mineralogy and petrology

HKE02 and HKE03 are spinel-rich FGIs in the same polished section of Efremovka with maximum dimensions corresponding to ~1.7 mm and ~0.9 mm, respectively (Fig. 1). The FGIs are located near an FTA CAI HKE01 (Fig. 1a; Kawasaki et al., 2012, 2019). Both spinel-rich FGIs exhibit irregular shapes and similar complex multi-layered textures that are mainly composed of spinel, melilite, and diopside (Fig. 2). Crystal sizes of the constituent minerals are mainly a few micrometers across and generally less than 10 μm across for the both spinel-rich FGIs (Fig. 2b and 2d). The textures are consistent with those of previously reported spinel-rich FGIs from the reduced CV chondrites (Krot et al., 2004a). The bulk ^{27}Al/^{24}Mg ratios of HKE02 and HKE03 are estimated as 2.9 and 2.7, respectively. A detailed mineralogical description of HKE02 is presented by Kawasaki et al. (2019).

HKV03 is a spinel-rich FGI in the polished section of Vigarano with a maximum dimension of ~3 mm (Fig. 3), located near the FTA CAI V2-01 (Katayama et al., 2012; Kawasaki et al., 2017, 2019). HKV03 exhibits a highly irregular shape and is composed of nodules with multi-layered textures of spinel, melilite, and thin diopside, from their core to rim (Fig. 3b). Anorthite is occasionally observed between the melilite layer and diopside layer. Individual nodules with sizes of several micrometers to several tens of micrometers are not always directly attached to each other and are mainly separated by matrix minerals. The crystal sizes of the constituent minerals are mainly a few micrometers across and are generally less than 10 μm across. Hibonite and perovskite are observed as accessory minerals. The bulk ^{27}Al/^{24}Mg ratio of HKV03 could not be determined owing to complex textures.

The reduced CV chondrite TIL 07007 contains numerous pristine FGIs (Kim and Choi, 2016). TIL01 is a spinel-rich FGI in the polished thin section of TIL 07007 with a maximum dimension of ~1.3 mm (Fig. 4). On the polished thin section, TIL01 appears as being separated into two inclusions (Fig. 4a). However, the two islands are petrographically very similar to each other such that they are extremely likely to correspond to a single FGI. In a manner similar to the spinel-rich FGIs HKE02 and HKE03, TIL01 exhibits an irregular shape and complex multi-layered textures that are mainly composed of spinel, melilite, and diopside (Fig. 4b). Crystal sizes of the constituent minerals are mainly a few micrometers across and generally less than 10 μm across. The bulk ^{27}Al/^{24}Mg ratio of TIL01 is estimated as 2.6.

TIL02 in the polished thin section of TIL 07007 consists of fine-grained anorthite-pyroxene-rich core enclosed by FTA CAI-like melilite-rich mantle, with a maximum dimension of ~3.4 mm (Fig. 5). The FTA CAI-like melilite-rich mantle is surrounded by a Wark–Lovering rim that is composed of spinel, anorthite, and diopside
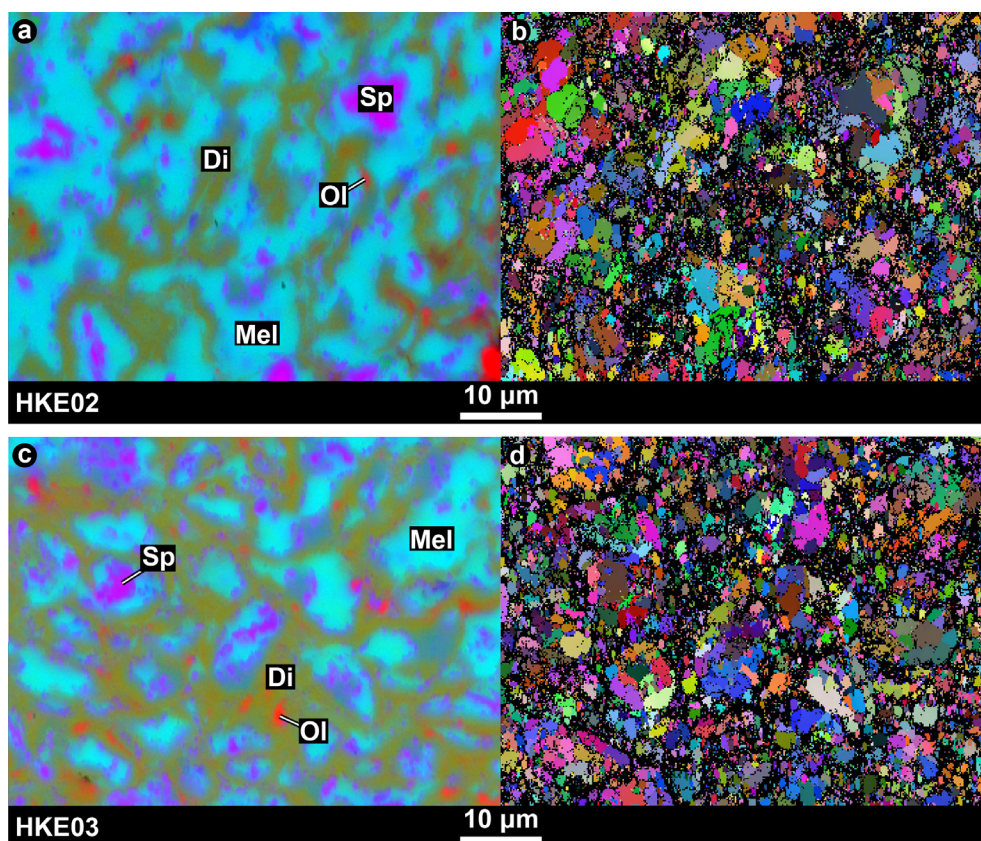
Fig. 2. Representative textures of (a, b) *HKE02* and (c, d) *HKE03*. (a) Combined X-ray elemental map in the area indicated by the yellow box in Fig. 1b denoting Mg (red), Ca (green), and Al (blue). (b) Electron backscatter diffraction (EBSD) Euler map of the same area shown in (a). (c) Combined X-ray elemental map in the area indicated by the yellow box in Fig. 1c denoting Mg (red), Ca (green), and Al (blue). (d) Electron backscatter diffraction (EBSD) Euler map of the same area displayed in (c). All the maps exhibit the same field of view. Di, diopside; Mel, melilite; Ol, olivine; Sp, spinel. (For interpretation of the references to colour in this figure legend, the reader is referred to the web version of this article.)

(Fig. 5b, Wark and Lovering, 1977). The anorthite-pyroxene-rich core part is composed of mineral layers of anorthite and diopside with fewer amounts of melilite and spinel (Fig. 5b and c). The anorthite crystals in the core part have grain sizes of typically several micrometers across and generally less than 10 μm across (Fig. 5c and d). Spinel crystals with sizes of ~1 μm are often observed in melilite crystals and at grain boundaries of anorthite and melilite (Fig. 5c and d). The bulk $^{27}Al/^{24}Mg$ ratio of *TIL02* is estimated as 5.4.

TIL03 in the polished thin section of TIL 07007 is an intermediate object between spinel-rich FGIs and amoeboid olivine aggregates (AOAs), with a maximum dimension of ~6 mm (Fig. 6). *TIL03* exhibits an irregular shape and is petrographically divided into core and mantle parts. The core part exhibits complex multi-layered textures composed mainly of spinel, anorthite, diopside, and forsteritic olivine (Fig. 6b). The mantle part contains melilite and more abundant olivine than the core part and olivine grains also form the accretionary rim (Fig. 6c, e.g., Krot et al., 2004b). The bulk $^{27}Al/^{24}Mg$ ratio of *TIL03* is estimated as 0.7. *TIL03* does not belong to either typical FGIs and AOAs and is chemically intermediate between them.

HKD01 in the polished thin section of NWA 8613 is a hibonite-rich FGI, which exhibits an irregular shape with a maximum dimension of ~12 mm (Fig. 7). *HKD01* is composed mainly of melilite, hibonite, and spinel with crystal sizes of generally less than ~10 μm across with the exception of lath shaped hibonite crystals with sizes of typically a few tens of micrometers. *HKD01* is petrographically divided into hibonite-spinel-rich core and melilite-rich mantle parts. The entire inclusion is rimmed by a mineral layer of hibonite, spinel and diopside. The bulk $^{27}Al/^{24}Mg$ ratio of *HKD01* is estimated as 4.8.

3.2. Al–Mg isotopic compositions

The Mg-isotopic compositions and $^{27}Al/^{24}Mg$ ratios measured for minerals in the FGIs are summarized in Table 1 and plotted on $^{26}Al–^{26}Mg$ evolution diagrams in Fig. 8. The Al–Mg isotope data of *HKE02* are obtained from Kawasaki et al. (2019). The data for each FGI with the exception of *TIL02* yield very well-correlated $^{26}Al–^{26}Mg$ mineral isochrons. The Al–Mg isotope data for melilite and spinel in *TIL02* plot within the error on a single straight line on $^{26}Al–^{26}Mg$ evolution diagram
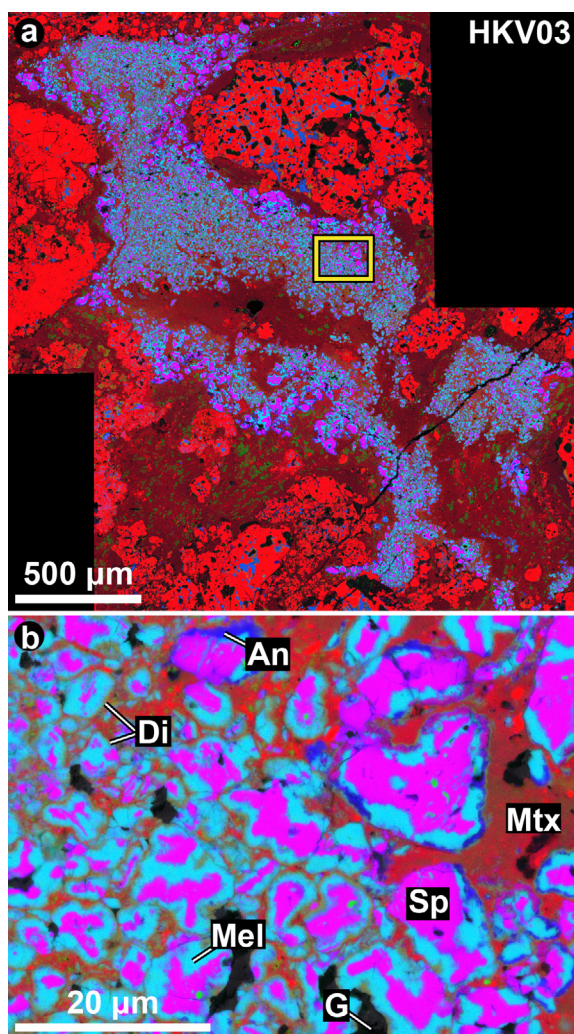
Fig. 3. Combined X-ray elemental maps of fine-grained CAI *HKV03* from Vigarano denoting Mg (red), Ca (green), and Al (blue). The yellow box in (a) indicates the area shown in (b). An, Anorthite; Di, diopside; G, gold coating residues; Mtx, matrix; Mel, melilite; Sp, spinel. Corresponding back scattered electron images are shown in Fig. S2. (For interpretation of the references to colour in this figure legend, the reader is referred to the web version of this article.)

Fig. 4. Combined X-ray elemental maps of fine-grained CAI *TIL01* from Theil Mountains 07007 denoting Mg (red), Ca (green), and Al (blue). The yellow box in (a) indicates the area shown in (b). Di, diopside; Mel, melilite; Ol, olivine; Sp, spinel. Corresponding back scattered electron images are shown in Fig. S3. (For interpretation of the references to colour in this figure legend, the reader is referred to the web version of this article.)

(Fig. 8f) while the anorthite data scatter significantly below the line (Fig. 8e). We define an $^{26}Al-^{26}Mg$ mineral isochron of *TIL02* using melilite and spinel data (Fig. 8f) without anorthite data (see discussion below). Inferred $(^{26}Al/^{27}Al)_0$ and initial $\delta^{26}Mg^*$ values, $(\delta^{26}Mg^*)_0$, for each of the FGI are summarized in Table 2. The $\delta^{26}Mg^*$ data calculated using the exponent 0.511 in the kinetic fractionation law (e.g., Jacobsen et al., 2008; Larsen et al., 2011; Wasserburg et al., 2012) and initial values using those values are listed in supplementary materials (Tables S1 and S2). The choice of exponents is insignificant for discussion in this paper because the changes in $\delta^{26}Mg^*$ values and initial values are significantly lower than the analytical errors.

Averaged $\delta^{25}Mg$ values of minerals in FGIs are 0.8 ± 2.5‰ (2SD) for melilite and spinel in *HKE02*, 0.8 ± 1.9‰ for melilite and spinel in *HKE03*, 1.0 ± 1.4‰ for melilite and spinel in *HKV03*, 1.1 ± 1.4‰ for melilite and spinel in *TIL01*, 0.0 ± 2.0‰ for melilite and spinel in *TIL02*, –2.2 ± 7.8‰ for anorthite in *TIL02*, 0.7 ± 2.1‰ for melilite and olivine in *TIL03*, and 1.1 ± 2.7‰ for melilite and spinel in *HKD01*, respectively. The $\delta^{25}Mg$ values of the FGI minerals are generally ∼0–1‰, although those of anorthite in *TIL02* exhibit large analytical errors compared with the other minerals.

4. DISCUSSION

4.1. Al–Mg isotope systematics

4.1.1. Disturbances of Al–Mg system for anorthite in fine-grained CAI TIL02

The Al–Mg systematics of *TIL02* is disturbed from a single straight line, i.e., the anorthite data scatter below
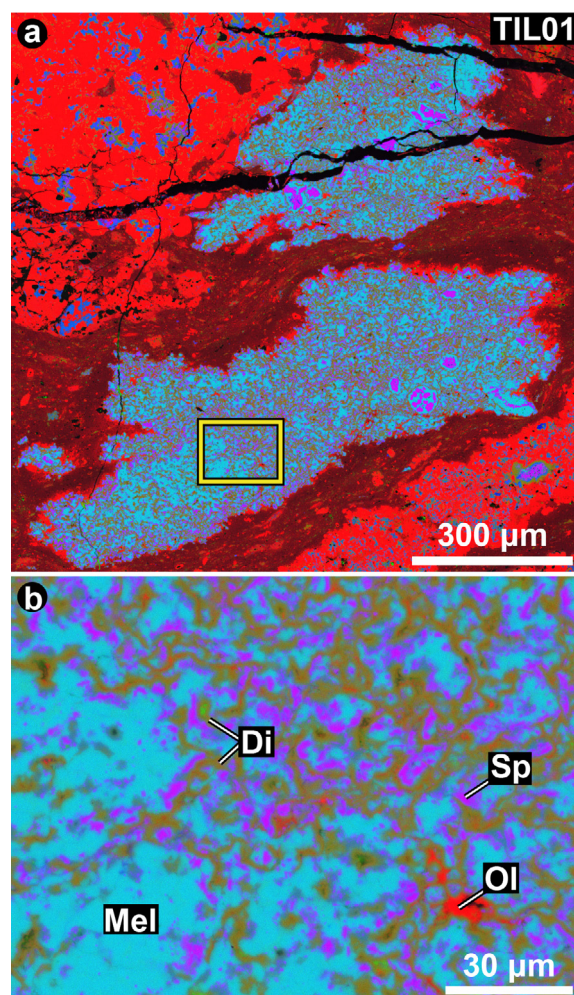
Fig. 5. (a–c) Combined X-ray elemental maps of fine-grained CAI *TIL02* from Theil Mountains 07007 denoting Mg (red), Ca (green), and Al (blue). The yellow box in (a) indicates the area shown in (b). The yellow box in (b) indicates the area shown in (c). (d) EBSD Euler map of the same area displayed in (c). An, anorthite; Di, diopside; Mtx, matrix; Mel, melilite; Sp, spinel. Corresponding back scattered electron images are shown in Fig. S4. (For interpretation of the references to colour in this figure legend, the reader is referred to the web version of this article.)
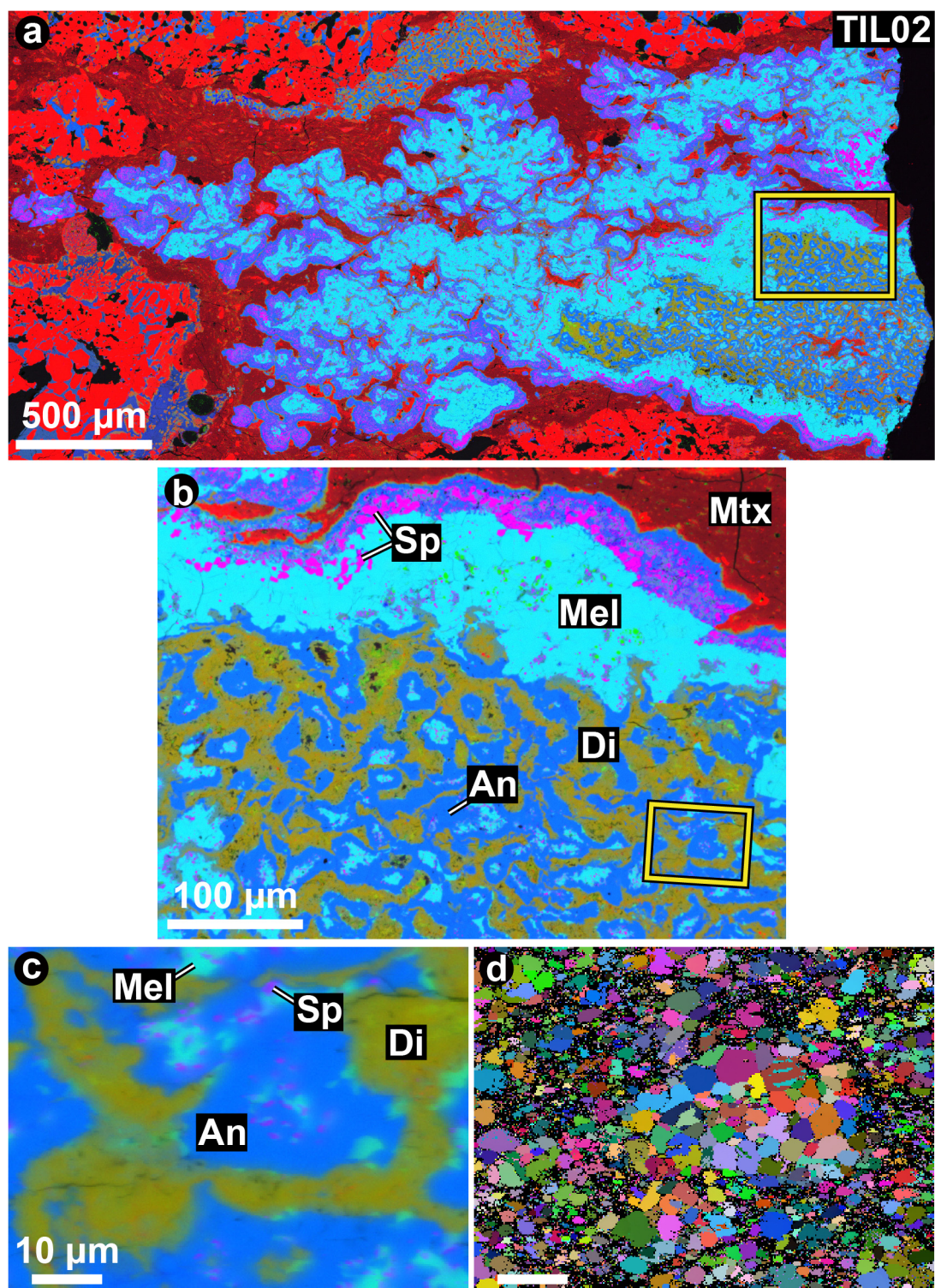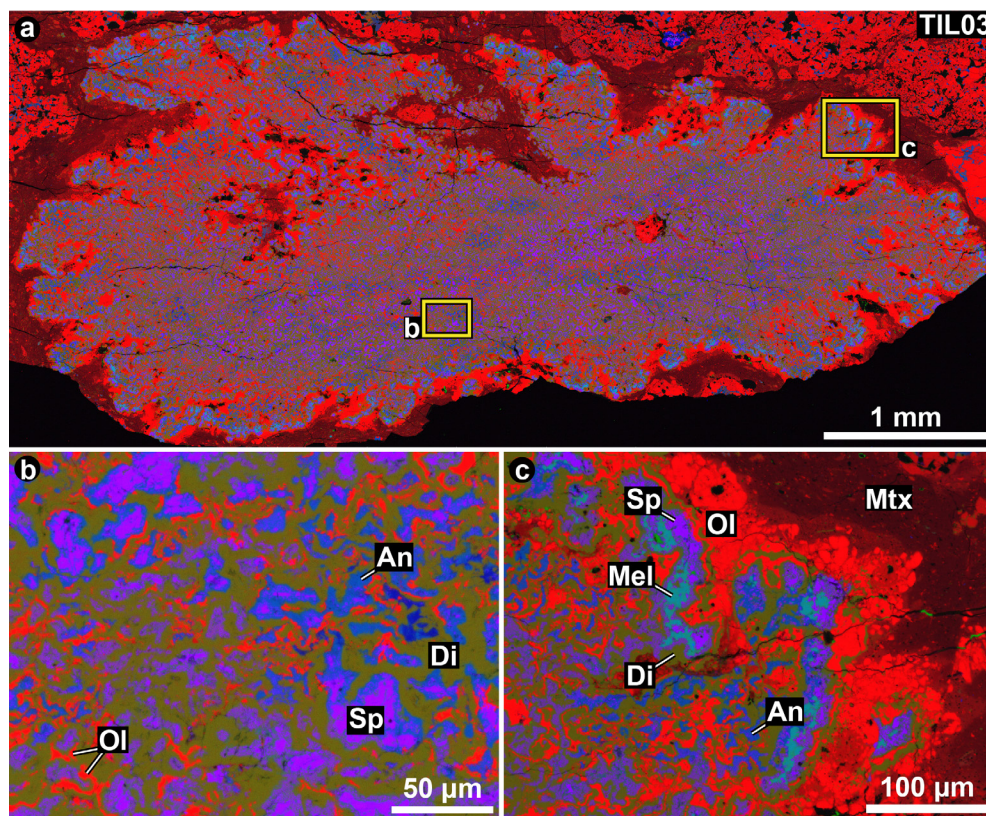
Fig. 6. (a) Combined X-ray elemental maps of fine-grained CAI *TIL03* from Theil Mountains 07007 denoting Mg (red), Ca (green), and Al (blue). (b) Magnified elemental map of the area as indicated by box (b) in (a). (c) Magnified elemental map of the area indicated by box (c) in (a). An, anorthite; Di, diopside; Mtx, matrix; Mel, melilite; Ol, olivine; Sp, spinel. Corresponding back scattered electron images are shown in Fig. S5. (For interpretation of the references to colour in this figure legend, the reader is referred to the web version of this article.)
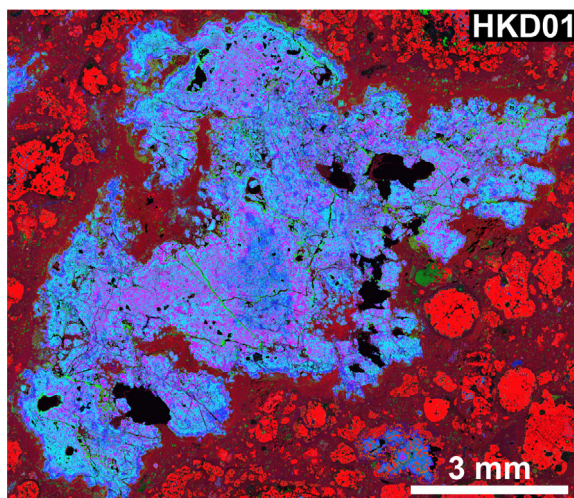

Fig. 7. (a) Combined X-ray elemental map of fine-grained CAI *HKD01* from Northwest Africa 8613 indicating Mg (red), Ca (green), and Al (blue). A corresponding back scattered electron image is shown in Fig. S6. (For interpretation of the references to colour in this figure legend, the reader is referred to the web version of this article.)

the mineral isochron defined by the melilite and spinel data (Fig. 8e). If we estimate slopes forced through an initial Mg-isotope ratio of $\delta^{26}Mg^* = 0$ at $^{27}Al/^{24}Mg = 0$ for each analysis of the anorthite, then they exhibit apparent initial values of $(^{26}Al/^{27}Al)_0$ ranging from $(1.1 \pm 0.5) \times 10^{-6}$ to $(1.77 \pm 0.06) \times 10^{-5}$.

The Al–Mg systems of anorthite in many coarse-grained CAIs from Allende, Efremovka, and Vigarano are considered to have been disturbed by solid-state diffusion of Mg in the anorthite after ^{26}Al decay during metamorphism on the asteroidal parent body (e.g., Yurimoto et al., 2000; Fagan et al., 2007; Ito and Messenger, 2010; MacPherson et al., 2012; Kawasaki et al., 2015, 2018; Aléon et al., 2018). The disturbance processes of Al–Mg system for CAI minerals are controlled by the self-diffusion rates of Mg in the minerals as well as their grain sizes, textural relationships, and chemical and Mg-isotopic compositions within and between minerals (e.g., Yurimoto et al., 2000; Kawasaki et al., 2015, 2018). Kawasaki et al. (2015) demonstrated Mg-isotope exchange between anorthite and spinel resulting in resetting of the Al–Mg system for anorthite in Allende Type C CAI *EK1-04–2* by quantifications of those controlling factors.

The anorthite measured for Al–Mg isotopes is located in the core part of *TIL02* and exhibits grain sizes of typically

Table 1

Magnesium isotopic compositions (‰) and $^{27}Al/^{24}Mg$ ratios of minerals in fine-grained CAIs.

Minerals	$^{27}Al/^{24}Mg$	2σ	$\delta^{26}Mg^*$	2σ	$\delta^{25}Mg$	2σ
HKE03						
Mel	29.2	0.3	7.5	1.3	2.1	1.7
Mel	40.8	1.1	9.9	1.5	−0.1	1.8
Mel	49.7	0.3	11.8	1.8	0.4	1.8
Mel	46.6	0.6	12.2	1.6	−0.5	1.3
Mel	32.9	0.4	7.3	1.4	2.0	1.1
Mel	28.8	0.3	6.6	1.2	0.7	0.8
Mel	56.1	0.6	13.7	1.5	0.7	1.3
Sp	2.582	0.004	0.69	0.11	1.05	0.06
HKV03						
Mel	51.9	1.4	18.9	2.0	0.8	1.2
Mel	32.0	0.3	11.3	1.6	1.2	1.0
Mel	82.8	3.3	31.1	2.4	1.1	1.3
Mel	40.3	0.5	14.5	1.9	2.3	1.3
Mel	56.5	0.9	20.3	1.7	0.0	1.1
Mel	133.0	2.3	46.8	3.2	0.8	2.0
Mel	57.7	1.1	20.6	1.9	2.2	1.4
Mel	62.2	0.5	21.3	2.2	0.5	1.4
Sp	2.513	0.004	0.92	0.13	0.79	0.09
Sp	2.519	0.004	0.93	0.18	0.78	0.09
Sp	2.530	0.004	0.85	0.13	1.03	0.09
Sp	2.503	0.004	0.80	0.14	0.26	0.10
TIL01						
Mel	21.7	0.5	6.1	1.3	−0.5	1.1
Mel	18.0	0.4	5.3	1.1	1.1	1.0
Mel	28.1	0.1	8.5	2.0	1.3	1.3
Mel	30.1	0.5	9.8	1.7	1.2	1.4
Mel	34.6	0.5	11.5	1.3	0.9	1.3
Mel	19.2	0.1	5.6	1.1	2.1	1.3
Mel	26.8	0.1	9.0	1.3	0.9	1.3
Sp	2.584	0.009	0.73	0.14	1.18	0.08
Sp	2.591	0.009	0.84	0.12	1.49	0.07
TIL02						
An	1839	48	234.2	8.1	2.2	3.9
An	3415	131	46.5	9.0	1.5	5.5
An	1050	19	8.2	4.7	−6.2	2.8
An	1436	32	60.0	5.6	−3.1	3.3
An	3855	121	38.3	10.3	−5.5	5.3
Mel	29.3	0.1	10.2	1.3	−0.3	1.1
Mel	57.8	0.2	18.2	1.9	0.1	1.4
Mel	24.1	0.1	8.1	1.4	0.2	1.2
Mel	48.8	0.2	16.6	1.7	−0.4	1.3
Mel	45.4	0.3	15.5	1.7	−2.5	1.2
Mel	55.3	0.3	17.5	1.4	0.0	1.2
Mel	21.6	0.1	6.6	1.1	0.9	1.1
Mel	22.5	0.1	7.0	1.1	0.8	1.3
Mel	40.0	0.3	12.6	1.9	−0.6	1.5
Sp	2.495	0.002	0.81	0.09	0.85	0.08
Sp	2.486	0.001	0.78	0.09	0.79	0.10
TIL03						
Mel	42.6	0.7	13.1	1.9	−0.1	1.4
Mel	22.7	0.1	5.6	1.5	2.3	1.3
Mel	30.6	0.3	8.8	1.4	0.2	1.1
Mel	55.4	1.0	16.1	1.8	2.8	1.2
Mel	14.2	0.0	4.4	1.1	1.2	0.9
Mel	31.4	0.2	9.8	1.2	0.9	1.0
Mel	40.4	0.9	11.6	1.2	0.7	0.9
Ol	0.0009	0.0001	0.02	0.09	−0.39	0.07
Ol	0.0001	0.0000	−0.03	0.09	−0.09	0.05

Ol	0.0002	0.0000	−0.03	0.09	0.17	0.05
Ol	0.0002	0.0000	0.00	0.10	0.10	0.06
HKD01						
Mel	225.1	3.9	76.5	3.2	1.2	1.6
Mel	272.7	0.7	95.9	3.8	3.0	2.2
Mel	152.6	0.4	52.7	2.5	−0.5	1.2
Mel	139.7	1.2	47.7	2.9	2.9	2.0
Mel	59.5	0.6	19.8	1.7	−0.9	1.7
Mel	61.4	0.2	21.6	1.9	−0.5	1.7
Mel	145.6	2.4	51.0	2.5	0.9	1.3
Mel	120.2	0.5	41.7	2.4	1.3	1.2
Mel	85.3	0.2	27.9	2.5	0.8	1.9
Sp	2.521	0.002	0.82	0.11	0.45	0.15
Sp	2.518	0.002	0.81	0.14	0.09	0.14
Sp	2.506	0.001	0.75	0.12	2.55	0.15
Sp	2.512	0.001	0.85	0.11	2.62	0.15

An: anorthite, Mel: melilite, Ol: olivine, Sp: spinel.

several micrometers across and generally less than 10 μm across (Fig. 5c and d). Spinel crystals with sizes of ∼1 μm are often observed at grain boundaries of the anorthite. Based on the calculation by Kawasaki et al. (2015) using self-diffusion coefficients of Mg-isotopes in spinel (Sheng et al., 1992; Liermann and Ganguly, 2002) and in anorthite (LaTourrette and Wasserburg, 1998), if Mg-isotopes in 10 μm-sized anorthite grains are equilibrated by diffusion, then Mg-isotope equilibrium is also achieved in 1 μm-sized spinel grains. In order for re-equilibration of Mg-isotopes in 10 μm-sized anorthite grains within a time-scale of 1–10 Myr, required temperatures could be calculated to be higher than ∼650–700 K. The exchange conditions, textural relationships, and anorthite Al–Mg isotope data suggest that the anorthite in the core part of *TIL02* partially exchanged their Mg-isotopes with the spinel grains by solid-state diffusion, and this could have occurred during metamorphism on the parent body, of which metamorphic temperatures may have been lower than ∼650–700 K. Given numbers of Mg atoms in the anorthite grain and spinel grain of *TIL02*, the spinel with 1/100 volume of the anorthite are sufficient to decrease $\delta^{26}Mg*$ for the anorthite to 1/10. Therefore, the Al–Mg isotope data for the anorthite in this study do not exhibit chronological significance due to incomplete resetting of the Al–Mg system with the exception of exhibiting evidence of live-^{26}Al at the CAI formation.

Given that the anorthite grains partially exchanged their Mg-isotopes, the diffusion distance of Mg-isotopes in the spinel grains of *TIL02* may be at most 1 μm scale. The spinel grains measured for Al–Mg isotopes are slightly larger than 10 μm in size, and thus the Al–Mg system could have remained isotopically closed starting from their formation within the measurement error. Similarly, the Al–Mg system for the melilite grains measured could also have remained isotopically closed from their formation within the measurement error.

4.1.2. Primitive signatures of $(^{26}Al/^{27}Al)_0$ for fine-grained CAIs from reduced CV chondrites

The Al–Mg isotopic compositions of spinel and melilite in the FGIs *HKE02*, *HKE03*, *HKV03*, *TIL01*, *TIL02* and

HKD01, and olivine and melilite in the FGI *TIL03* evidently exhibit an isochronous correlation between ^{27}Al/^{24}Mg and δ^{26}Mg*. The Al–Mg mineral isochrons of the seven FGIs are defined (Fig. 8). The inferred $(^{26}Al/^{27}Al)_0$ for *HKE02* and *HKV03* are essentially identical to the whole-rock CAI value of $(^{26}Al/^{27}Al)_0 \sim 5.2 \times 10^{-5}$ (Jacobsen et al., 2008; Larsen et al., 2011) within their errors while those for the other five FGIs are clearly lower than the whole-rock CAI value. The seven FGIs exhibit statistically significant variations in $(^{26}Al/^{27}Al)_0$, ranging from (5.19 ± 0.17) to $(3.35 \pm 0.21) \times 10^{-5}$.

The FGI *HKE02* exhibiting the highest $(^{26}Al/^{27}Al)_0$ of $(5.19 \pm 0.17) \times 10^{-5}$ and FGI *HKE03* exhibiting the lowest $(^{26}Al/^{27}Al)_0$ of $(3.35 \pm 0.21) \times 10^{-5}$ are included in the same polished section of Efremovka (Fig. 1). The two spinel-rich FGIs exhibit similar mineralogical textures. They are composed mainly of mineral layers of spinel, melilite, and diopside (Fig. 2a and c). The crystal sizes of the constituent minerals are mainly a few micrometers across and are generally less than 10 μm across for the both FGIs (Fig. 2b and d). The re-equilibrium processes of the Al–Mg system for CAI minerals are controlled by textural relationships and Al–Mg isotopic compositions of the minerals (e.g., Kawasaki et al., 2015); thus, the observations strongly suggest that the difference in $(^{26}Al/^{27}Al)_0$ between them does not originate from late disturbances of the Al–Mg system on the parent body. Therefore, the observed variations in $(^{26}Al/^{27}Al)_0$ among the FGIs are most likely to reflect variations in $(^{26}Al/^{27}Al)_0$ acquired at nebular thermal processes (i.e., condensation) in the earliest Solar System. Similar, albeit slightly smaller, variations ranging from (5.05 ± 0.18) to $(4.08 \pm 0.75) \times 10^{-5}$ were reported for individual FGIs in some of the most pristine carbonaceous chondrites, Acfer 094 (C-ungrouped) and Yamato-81020 (CO) (Ushikubo et al., 2017).

4.2. $(^{26}Al/^{27}Al)_0$ and $(\delta^{26}Mg*)_0$ for fine-grained CAIs

It is still debatable whether variations in $(^{26}Al/^{27}Al)_0$ observed among CAIs correspond to a formation age spread or heterogeneous distributions of ^{26}Al/^{27}Al ratios in the forming region, or both. (e.g., Wasserburg et al., 1977;

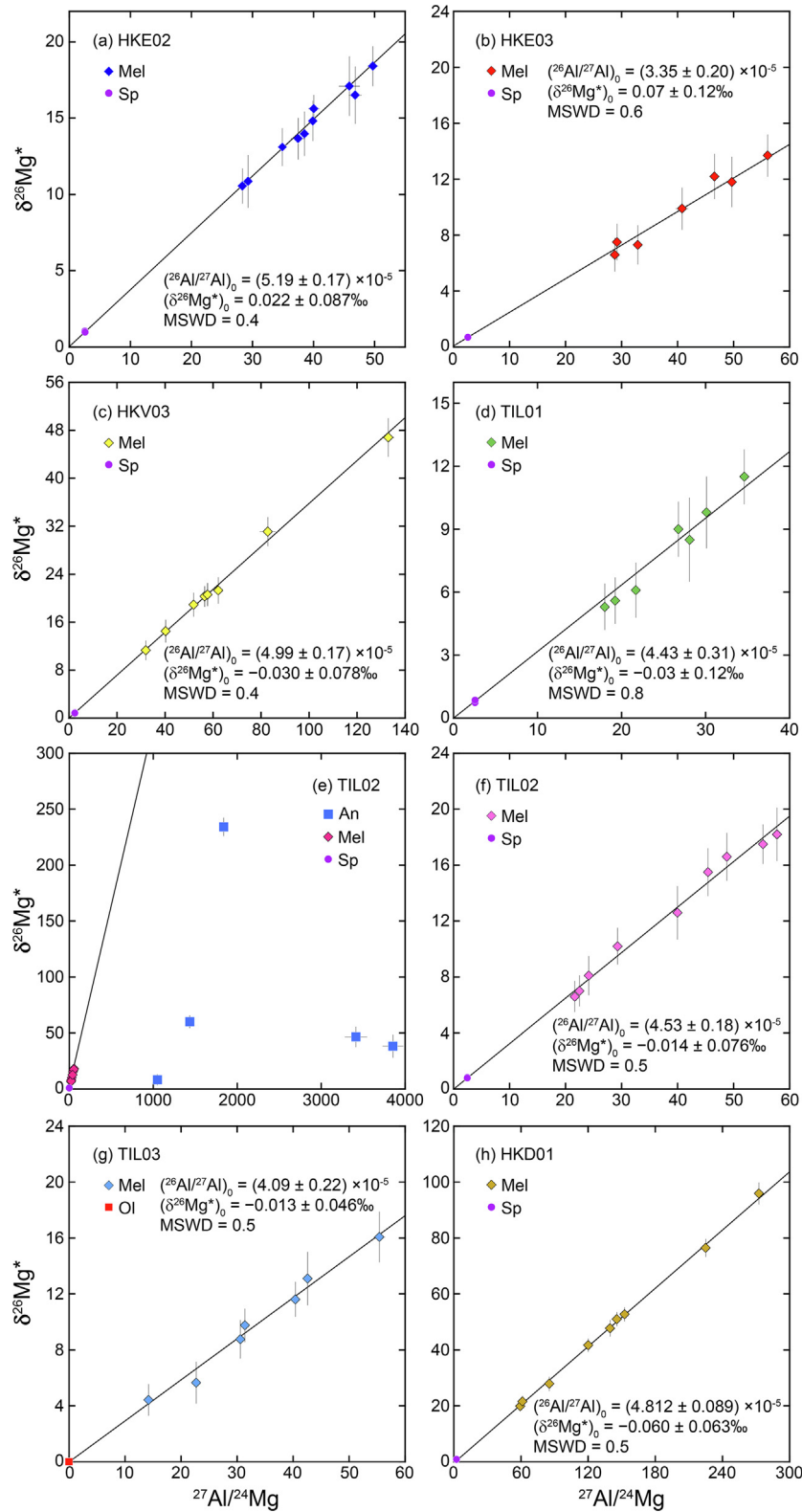Fig. 8. ^{26}Al–^{26}Mg mineral isochrons for fine-grained CAIs from reduced CV chondrites, (a) *HKE02*, (b) *HKE03*, (c) *HKV03*, (d) *TIL01*, (e, f) *TIL02*, (g) *TIL03*, and (h) *HKD01*. (f) shows data with low ^{27}Al/^{24}Mg ratio in (e). Al–Mg isotope data for (a) *HKE02* are obtained from Kawasaki et al. (2019). Isoplot Model 1 (Ludwig, 2003) is used to fit isochrons. Errors correspond to 2σ. Symbols without error bars exhibit errors smaller than their symbol sizes. An, anorthite; Mel, melilite; Ol, olivine; Sp, spinel.

Table 2
Summary of $(^{26}Al/^{27}Al)_0$, $(\delta^{26}Mg^*)_0$ and bulk $^{27}Al/^{24}Mg$ for each fine-grained CAI.

CAI	Meteorite	$(^{26}Al/^{27}Al)_0$	2σ	$(\delta^{26}Mg^*)_0$	2σ	bulk $^{27}Al/^{24}Mg$
HKE02[a]	Efremovka	5.19×10^{-5}	0.17×10^{-5}	0.022	0.087	2.9
HKE03	Efremovka	3.35×10^{-5}	0.20×10^{-5}	0.07	0.12	2.7
HKV03	Vigarano	4.99×10^{-5}	0.17×10^{-5}	-0.030	0.078	n.a.
TIL01	Thiel Mountains 07007	4.43×10^{-5}	0.31×10^{-5}	-0.03	0.12	2.6
TIL02	Thiel Mountains 07007	4.53×10^{-5}	0.18×10^{-5}	-0.014	0.076	5.4
TIL03	Thiel Mountains 07007	4.09×10^{-5}	0.22×10^{-5}	-0.013	0.046	0.7
HKD01	Northwest Africa 8613	4.812×10^{-5}	0.089×10^{-5}	-0.060	0.063	4.8

n.a.: not analyzed.
[a] From Kawasaki et al. (2019).

Krot et al., 2008, 2012; Jacobsen et al., 2008; Larsen et al., 2011; Makide et al., 2011; Holst et al., 2013; Kööp et al., 2016; Park et al., 2017; Kawasaki et al., 2019 and references therein). The debate can be clarified if precisions of $(\delta^{26}Mg^*)_0$ and $(^{26}Al/^{27}Al)_0$ are sufficiently high because $(\delta^{26}Mg^*)_0$ increases with time depending on the $^{26}Al/^{24}Mg$ ratio (Fig. 9). However, the variations in $(\delta^{26}Mg^*)_0$ among the FGIs in this study are not resolvable even if applying the smallest analytical error (0.046‰), which is one of the smallest errors for mineral isochron studies so far. We cannot rule out the view of heterogeneous distributions of ^{26}Al in the forming region of FGIs. If this is the case, then the data imply heterogeneous distributions of ^{26}Al in the CV CAI-forming region corresponding to a range of over at least $3.4 \times 10^{-5} < (^{26}Al/^{27}Al)_0 < 5.2 \times 10^{-5}$.

Conversely, on the Mg-isotope evolution diagram (Fig. 9), the data of FGIs plot on the Mg-isotope evolution curve of solar-composition gas within the errors, thereby suggesting that their $(^{26}Al/^{27}Al)_0$ correspond to a formation age spread and their condensation occurred from the solar-composition nebular gas. The FGIs cannot be formed via recondensation of their evaporation gas or from Al/Mg fractionated nebular gas formed at the age corresponding $(^{26}Al/^{27}Al)_0$ of $\sim5.2 \times 10^{-5}$ (Jacobsen et al., 2008; Larsen et al., 2011) because the FGI data clearly deviate from the Mg-isotope evolution curves of the fractionated Al/Mg ratio materials (Fig. 9). Note that the heterogeneity of $^{26}Mg/^{24}Mg$ in the CAI-forming region has also been suggested (e.g., Wasserburg et al., 2012; Larsen et al., 2020). The inferred $(\delta^{26}Mg^*)_0$ for formation reservoirs of some of CV CAIs and CAIs of CR chondrites, $-0.095 \pm 0.026‰$ (Larsen et al., 2020), is lower than that for most of CV CAIs, $-0.0159 \pm 0.0014‰$ (Larsen et al., 2011) or $-0.040 \pm 0.029‰$ (Jacobsen et al., 2008). Assuming precursors of the FGIs formed when $^{26}Al/^{27}Al$ was $(5.23 \pm 0.13) \times 10^{-5}$ (Jacobsen et al., 2008), the precursor $(\delta^{26}Mg^*)_0$ can be back-calculated to be $-0.29 \pm 0.13‰$ for HKE03, $-0.18 \pm 0.14‰$ for TIL01, $-0.28 \pm 0.13‰$ for TIL02, $-0.07 \pm 0.06‰$ for TIL03, and $-0.20 \pm 0.09‰$ for HKD01. Some of the back-calculated $(\delta^{26}Mg^*)_0$ are clearly lower than the any inferred $(\delta^{26}Mg^*)_0$ values for CAI-formation reservoirs above. Rather, such large negative $(\delta^{26}Mg^*)_0$ values have been recognized only for FUN CAIs (e.g., Park et al., 2017 and references therein), although the observed variations of mass-dependent magnesium isotope
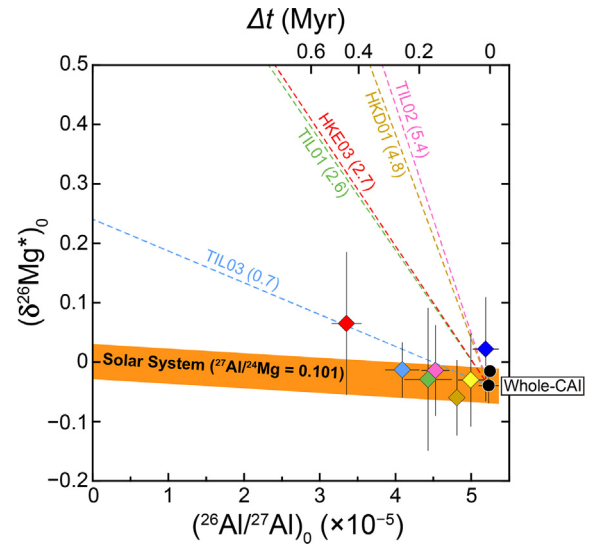

Fig. 9. Mg-isotope evolution of fine-grained CAIs from reduced CV chondrites. Mg-isotope evolution curves starting from whole-rock CAI $(^{26}Al/^{27}Al)_0$ and $(\delta^{26}Mg^*)_0$ values (black circles, Jacobsen et al., 2008; Larsen et al., 2011) are depicted by colored dotted lines for fine-grained CAIs HKE03 $(^{27}Al/^{24}Mg = 2.7)$, TIL01 $(^{27}Al/^{24}Mg = 2.6)$, TIL02 $(^{27}Al/^{24}Mg = 5.4)$, TIL03 $(^{27}Al/^{24}Mg = 0.7)$, and HKD01 $(^{27}Al/^{24}Mg = 4.8)$, and by an orange-colored thick line for a solar-composition gas $(^{27}Al/^{24}Mg = 0.101)$. If Al/Mg chemical fractionations for the fine-grained CAIs occurred at the formation time of canonical CAIs, then Mg-isotopic compositions of the fine-grained CAIs may have individually evolved by their bulk $^{27}Al/^{24}Mg$ ratios along the colored dotted lines. Conversely, if the CAIs condensed from the solar-composition gas, then their Mg-isotopic compositions would be plotted within the orange-colored thick line. Note that the Mg-isotope evolution curves are drawn using the whole-rock CAI values by Jacobsen et al. (2008), because the values reported by Jacobsen et al. (2008) entirely cover those of Larsen et al. (2011) due to larger analytical errors. Colored diamonds correspond to inferred $(^{26}Al/^{27}Al)_0$ and $(\delta^{26}Mg^*)_0$ values of the fine-grained CAIs. The $^{27}Al/^{24}Mg$ ratio of the Solar System is obtained from Lodders (2003). Errors are 2σ. (For interpretation of the references to colour in this figure legend, the reader is referred to the web version of this article.)

fractionation for the FGIs are very small ($\delta^{25}Mg \sim$0–1‰). These simulations further support Al/Mg chemical fractionation events for the FGIs did not occur at the

formation age of canonical CAIs and they formed from the evolved solar-composition nebular gas (Fig. 9). The formation age spread corresponds to 0.44 ± 0.07 Myr at the very beginning of the Solar System.

The variations in $(^{26}Al/^{27}Al)_0$ observed among the FGIs in this study are essentially similar to those for coarse-grained, igneous CAIs and FTA CAIs in CV chondrites (Fig. 10, Kita et al., 2012; MacPherson et al., 2012, 2017, 2018; Kawasaki et al., 2017, 2018, 2019). Among them,
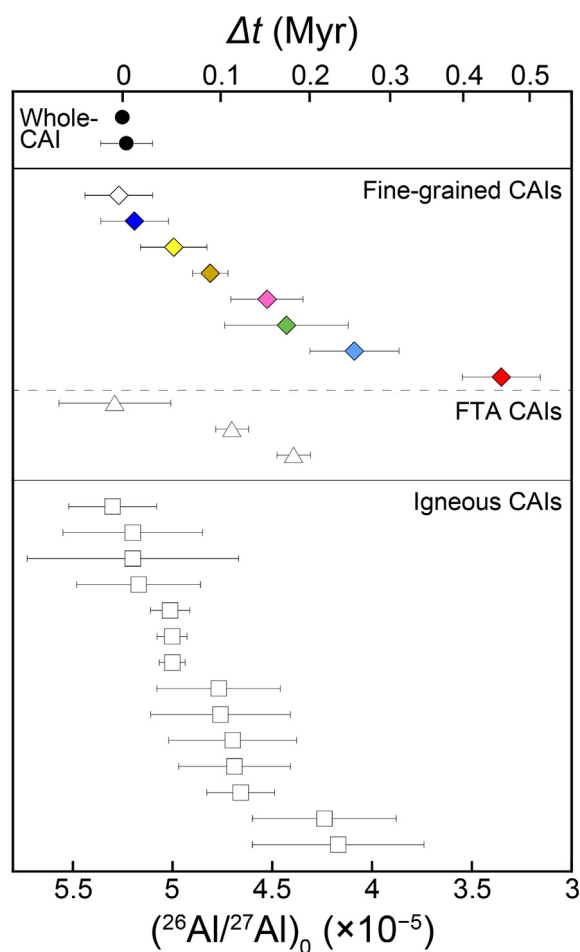

Fig. 10. Variations in initial $^{26}Al/^{27}Al$ ratios for CAIs in CV chondrites as determined by high-precision mineral isochron studies. Initial $^{26}Al/^{27}Al$ ratios for fine-grained CAIs from MacPherson et al. (2010) (open diamond) and this study (colored diamonds) are shown for *L3536, HKE02, HKV03, HKD01, TIL02, TIL01, TIL03,* and *HKE03*, from top to bottom. Initial $^{26}Al/^{27}Al$ ratios for fluffy Type A (FTA) CAIs from the literature (open triangles, from top to bottom) are shown for *F8, V2-01,* and *HKE01* (MacPherson et al., 2012; Kawasaki et al., 2017, 2019). Initial $^{26}Al/^{27}Al$ ratios for igneous CAIs from the literature are shown for *E60, E64, SJ101, F9, USNM 3898, TS34, L3535, F4, V3137, 4N, TS35, F1, F6,* and *ALVIN* (open squares, from top to bottom, Kita et al., 2012; MacPherson et al., 2012, 2017, 2018; Kawasaki et al., 2018). Whole-rock CAI initial $^{26}Al/^{27}Al$ ratios (black circles) are from Jacobsen et al. (2008) and Larsen et al. (2011). Errors correspond to 2σ. (For interpretation of the references to colour in this figure legend, the reader is referred to the web version of this article.)

the igneous CAIs can potentially have a significant age spread, given that the relative age of the Allende Type B1 CAI TS34 from the formation of canonical CAIs (Jacobsen et al., 2008; Larsen et al., 2011) calculated from $(^{26}Al/^{27}Al)_0$ is consistent with the relative age calculated from $(\delta^{26}Mg^*)_0$ and bulk $^{27}Al/^{24}Mg$ (Kawasaki et al., 2018). Moreover, igneous CAIs exhibiting sub-canonical $(^{26}Al/^{27}Al)_0$ values display elevated positive $(\delta^{26}Mg^*)_0$ values (MacPherson et al. 2012; Kita et al., 2012). Therefore, if the formation regions of FGIs, igneous CAIs, and FTA CAIs in CV chondrites are identical, then our data indicate that the CV CAI formation continued for at least ∼0.4 Myr at the very beginning of the Solar System. The inferred period for the CV CAI formation can indicate either the time duration of refractory dust transportation processes from the CAI-forming region, which may correspond to the inner edge of the solar protoplanetary disk (Itoh and Yurimoto, 2003; Yurimoto et al., 2008), to a forming region of the CV chondrite parent body (e.g., Ciesla, 2010) or the time duration of occurrence of the CAI formation processes in the CAI-forming region.

5. CONCLUSIONS

In this study, high-precision Al–Mg mineral isochrons of seven FGIs from the reduced CV chondrites via *in situ* analysis with SIMS exhibited statistically significant variations in $(^{26}Al/^{27}Al)_0$ among FGIs, ranging from (5.19 ± 0.17) to $(3.35 \pm 0.21) \times 10^{-5}$. Two spinel-rich FGIs from Efremovka with similar mineralogical textures exhibit a highest $(^{26}Al/^{27}Al)_0$ of $(5.19 \pm 0.17) \times 10^{-5}$ and a lowest $(^{26}Al/^{27}Al)_0$ of $(3.35 \pm 0.21) \times 10^{-5}$. This indicates that the difference in $(^{26}Al/^{27}Al)_0$ between them does not originate from late disturbances of the Al–Mg system on the parent body. The inferred $(\delta^{26}Mg^*)_0$ values for FGIs are consistent with the Mg-isotope evolution of a solar-composition nebular gas. The Al–Mg data indicate that the FGIs formed from the solar-composition nebular gas over the period of 0.44 ± 0.07 Myr under the assumption of homogeneous distributions of ^{26}Al in the forming region. The observed variations in $(^{26}Al/^{27}Al)_0$ for FGIs are essentially similar to those for igneous CAIs in CV chondrites, thereby indicating that CAIs in CV chondrites have variations in $(^{26}Al/^{27}Al)_0$ from ∼5.2 to ∼3.4 × 10^{-5} despite their petrologic types and the formation processes they experienced. The data indicate that CAI-formation thermal processes—condensation and melting—occurred contemporaneously during ∼0.4 Myr at the very beginning of the Solar System, if ^{26}Al was distributed homogeneously in the forming region. Alternatively, the observed variations in $(^{26}Al/^{27}Al)_0$ indicate the possibility of heterogeneous distributions of ^{26}Al in the forming region, corresponding to a range of over at least $3.4 \times 10^{-5} < (^{26}Al/^{27}Al)_0 < 5.2 \times 10^{-5}$.

Declaration of Competing Interest

The authors declare that they have no known competing financial interests or personal relationships that could have appeared to influence the work reported in this paper.

APPENDIX A. SUPPLEMENTARY MATERIAL

Supplementary data to this article can be found online at https://doi.org/10.1016/j.gca.2020.03.045.

REFERENCES

Aléon J., Marin-Carbonne J., McKeegan K. D. and El Goresy A. (2018) O, Mg, and Si isotope distributions in the complex ultrarefractory CAI Efremovka 101.1: Assimilation of ultrarefractory, FUN, and regular CAI precursors. *Geochim. Cosmochim. Acta* **232**, 48–81.

Bollard J., Kawasaki N., Sakamoto N., Olsen M., Itoh S., Larsen K., Wielandt D., Schiller M., Connelly J. N., Yurimoto H. and Bizzarro M. (2019) Combined U-corrected Pb-Pb dating and ^{26}Al-^{26}Mg systematics of individual chondrules – Evidence for a reduced initial abundance of ^{26}Al amongst inner Solar System chondrules. *Geochim. Cosmochim. Acta* **260**, 62–83.

Boynton W. V. (1975) Fractionation in the solar nebula—Condensation of yttrium and the rare earth elements. *Geochim. Cosmochim. Acta* **39**, 569–584.

Catanzaro E. J., Murphy T. J., Garner E. L. and Shields W. R. (1966) Absolute isotopic abundance ratios and atomic weights of magnesium. *J. Res. Natl. Bur Stand.* **70a**, 453–458.

Ciesla F. J. (2010) The distributions and ages of refractory objects in the solar nebula. *Icarus* **208**, 455–467.

Connelly J. N., Bizzarro M., Krot A. N., Nordlund Å., Wielandt D. and Ivanova M. A. (2012) The absolute chronology and thermal processing of solids in the solar protoplanetary disk. *Science* **338**, 651–655.

Davis A. M. and Grossman L. (1979) Condensation and fractionation of rare earths in the solar nebula. *Geochim. Cosmochim. Acta* **43**, 1611–1632.

Davis A. M., Richter F. M., Mendybaev R. A., Janney P. E., Wadhwa M. and McKeegan K. D. (2015) Isotopic mass fractionation laws for magnesium and their effects on ^{26}Al–^{26}Mg systematics in solar system materials. *Geochim. Cosmochim. Acta* **158**, 245–261.

Fagan T. J., Guan Y. and MacPherson G. J. (2007) Al-Mg isotopic evidence for episodic alteration of Ca-Al-rich inclusions from Allende. *Meteorit. Planet. Sci.* **42**, 1221–1240.

Holst J. C., Olsen M. B., Paton C., Nagashima K., Schiller M., Wielandt D., Larsen K. K., Connelly J. N., Jorgensen J. K., Krot A. N., Nordlund A. and Bizzarro M. (2013) ^{182}Hf-^{182}W age dating of a ^{26}Al-poor inclusion and implications for the origin of short-lived radioisotopes in the early Solar System. *Proc. Natl. Acad. Sci. U. S. A.* **110**, 8819–8823.

Ito M. and Messenger S. (2010) Thermal metamorphic history of a Ca, Al-rich inclusion constrained by high spatial resolution Mg isotopic measurements with NanoSIMS 50L. *Meteorit. Planet. Sci.* **45**, 583–595.

Itoh S. and Yurimoto H. (2003) Contemporaneous formation of chondrules and refractory inclusions in the early solar system. *Nature* **423**, 728–731.

Itoh S., Makide K. and Yurimoto H. (2008) Calculation of radiogenic ^{26}Mg of CAI minerals under high precision isotope measurement by SIMS. *Appl. Surf. Sci.* **255**, 1476–1478.

Jacobsen B., Yin Q., Moynier F., Amelin Y., Krot A. N., Nagashima K., Hutcheon I. D. and Palme H. (2008) ^{26}Al-^{26}Mg and ^{207}Pb-^{206}Pb systematics of Allende CAIs: Canonical solar initial ^{26}Al/^{27}Al ratio reinstated. *Earth Planet. Sci. Lett.* **272**, 353–364.

Katayama J., Itoh S. and Yurimoto H. (2012) Oxygen isotopic zoning of reversely zoned melilite crystals in a Fluffy Type A Ca-Al-rich inclusion from the Vigarano meteorite. *Meteorit. Planet. Sci.* **47**, 2094–2106.

Kawasaki N., Sakamoto N. and Yurimoto H. (2012) Oxygen isotopic and chemical zoning of melilite crystals in a Type A Ca-Al-rich inclusion of Efremovka CV3 chondrite. *Meteorit. Planet. Sci.* **47**, 2084–2093.

Kawasaki N., Kato C., Itoh S., Wakaki S., Ito M. and Yurimoto H. (2015) ^{26}Al–^{26}Mg chronology and oxygen isotope distributions of multiple melting for a Type C CAI from Allende. *Geochim. Cosmochim. Acta* **169**, 99–114.

Kawasaki N., Itoh S., Sakamoto N. and Yurimoto H. (2017) Chronological study of oxygen isotope composition for the solar protoplanetary disk recorded in a fluffy Type A CAI from Vigarano. *Geochim. Cosmochim. Acta* **201**, 83–102.

Kawasaki N., Simon S. B., Grossman L., Sakamoto N. and Yurimoto H. (2018) Crystal growth and disequilibrium distribution of oxygen isotopes in an igneous Ca-Al-rich inclusion from the Allende carbonaceous chondrite. *Geochim. Cosmochim. Acta* **221**, 318–341.

Kawasaki N., Park C., Sakamoto N., Park S. Y., Kim H. N., Kuroda M. and Yurimoto H. (2019) Variations in initial ^{26}Al/^{27}Al ratios among fluffy Type A Ca–Al-rich inclusions from reduced CV chondrites. *Earth Planet. Sci. Lett.* **511**, 25–35.

Kim H. and Choi B.-G. (2016) Petrological characteristics of the fine-grained CAIs from the reduced CV chondrites Thiel Mountains 07003 and 07007, and origin of anorthite. (abstract #6290). *79th Annual Meeting of the Meteoritical Society*.

Kita N. T., Ushikubo T., Knight K. B., Mendybaev R. A., Davis A. M., Richter F. M. and Fournelle J. H. (2012) Internal ^{26}Al-^{26}Mg isotope systematics of a Type B CAI: Remelting of refractory precursor solids. *Geochim. Cosmochim. Acta* **86**, 37–51.

Kita N. T., Yin Q.-Z., MacPherson G. J., Ushikubo T., Jacobsen B., Nagashima K., Kurahashi E., Krot A. N. and Jacobsen S. B. (2013) ^{26}Al-^{26}Mg isotope systematics of the first solids in the early solar system. *Meteorit. Planet. Sci.* **48**, 1383–1400.

Kööp L., Davis A. M., Nakashima D., Park C., Krot A. N., Nagashima K., Tenner T. J., Heck P. R. and Kita N. T. (2016) A link between oxygen, calcium and titanium isotopes in ^{26}Al-poor hibonite-rich CAIs from Murchison and implications for the heterogeneity of dust reservoirs in the solar nebula. *Geochim. Cosmochim. Acta* **189**, 70–95.

Krot A. N., MacPherson G. J., Ulyanov A. A. and Petaev M. I. (2004a) Fine-grained, spinel-rich inclusions from the reduced CV chondrites Efremovka and Leoville: I. Mineralogy, petrology, and bulk chemistry. *Meteorit. Planet. Sci.* **39**, 1517–1553.

Krot A. N., Petaev M. I., Russell S. S., Itoh S., Fagan T. J., Yurimoto H., Chizmadia L., Weisberg M. K., Komatsu M., Ulyanov A. A. and Keil K. (2004b) Amoeboid olivine aggregates and related objects in carbonaceous chondrites: records of nebular and asteroid processes. *Chem. Erde* **64**, 185–239.

Krot A. N., Yurimoto H., Hutcheon I. D. and MacPherson G. J. (2005) Chronology of the early Solar System from chondrule-bearing calcium-aluminium-rich inclusions. *Nature* **434**, 998–1001.

Krot A. N., Yurimoto H., Hutcheon I. D., Chaussidon M., MacPherson G. J. and Paque J. (2007) Remelting of refractory inclusions in the chondrule-forming regions: Evidence from chondrule-bearing type C calcium-aluminum-rich inclusions from Allende. *Meteorit. Planet. Sci.* **42**, 1197–1219.

Krot A. N., Nagashima K., Bizzarro M., Huss G. R., Davis A. M., McKeegan K. D., Meyer B. S. and Ulyanov A. A. (2008) Multiple generations of refractory inclusions in the metal-rich carbonaceous chondrites Acfer 182/214 and Isheyevo. *Astrophys. J.* **672**, 713–721.

Krot A. N., Makide K., Nagashima K., Huss G. R., Ogliore R. C., Ciesla F. J., Yang L., Hellebrand E. and Gaidos E. (2012) Heterogeneous distribution of ^{26}Al at the birth of the solar system: Evidence from refractory grains and inclusions. *Meteorit. Planet. Sci.* **47**, 1948–1979.

Krot A. N. (2019) Refractory inclusions in carbonaceous chondrites: Records of early solar system processes. *Meteorit. Planet. Sci.* **54**, 1647–1691.

Larsen K. K., Trinquier A., Paton C., Schiller M., Wielandt D., Ivanova M. A., Connelly J. N., Nordlund Å., Krot A. N. and Bizzarro M. (2011) Evidence for magnesium isotope heterogeneity in the solar protoplanetary disk. *Astrophys. J. Lett.* **735**, L37–L43.

Larsen K. K., Wielandt D., Schiller M., Krot A. N. and Bizzarro M. (2020) Episodic formation of refractory inclusions in the Solar System and their presolar heritage. *Earth Planet. Sci. Lett.* **535**, 116088.

LaTourrette T. and Wasserburg G. J. (1998) Mg diffusion in anorthite: implications for the formation of early solar system planetesimals. *Earth Planet. Sci. Lett.* **158**, 91–108.

Lee T., Papanastassiou D. A. and Wasserburg G. J. (1976) Demonstration of Mg-26 excess in Allende and evidence for Al-26. *Geophys. Res. Lett.* **3**, 41–44.

Liermann H.-P. and Ganguly J. (2002) Diffusion kinetics of Fe^{2+} and Mg in aluminous spinel: Experimental determination and applications. *Geochim. Cosmochim. Acta* **66**, 2903–2913.

Lodders K. (2003) Solar system abundances and condensation temperatures of the elements. *Astrophys. J.* **591**, 1220–1247.

Ludwig K. (2003) ISOPLOT: A Geochronological Toolkit for Microsoft Excel 3.00. Berkeley Geochronological Center Special Publication No. 4, Berkeley, CA 94709.

MacPherson G. J. and Grossman L. (1981) A once-molten, coarse-grained, Ca-rich inclusion in Allende. *Earth Planet. Sci. Lett.* **52**, 16–24.

MacPherson G. J. and Grossman L. (1984) Fluffy Type A Ca-, Al-rich inclusions in the Allende meteorite. *Geochim. Cosmochim. Acta* **48**, 29–46.

MacPherson G. J., Davis A. M. and Zinner E. K. (1995) The distribution of aluminum-26 in the early Solar System-A reappraisal. *Meteoritics* **30**, 365–386.

MacPherson G. J., Bullock E. S., Janney P. E., Kita N. T., Ushikubo T., Davis A. M., Wadhwa M. and Krot A. N. (2010) Early solar nebular condensates with canonical, not supra-canonical, initial ^{26}Al/^{27}Al ratios. *Astrophys. J. Lett.* **711**, L117–L121.

MacPherson G. J., Kita N. T., Ushikubo T., Bullock E. S. and Davis A. M. (2012) Well-resolved variations in the formation ages for Ca-Al-rich inclusions in the early Solar System. *Earth Planet. Sci. Lett.* **331–332**, 43–54.

MacPherson G. J. (2014) Calcium-aluminum-rich inclusions in chondritic meteorites. In *Meteorites and Cosmochemical Processes. Treatise on Geochemistry*, vol. 1 (ed. A. M. Davis). Elsevier, Oxford, pp. 139–179.

MacPherson G. J., Bullock E. S., Tenner T. J., Nakashima D., Kita N. T., Ivanova M. A., Krot A. N., Petaev M. I. and Jacobsen S. B. (2017) High precision Al–Mg systematics of forsterite-bearing Type B CAIs from CV3 chondrites. *Geochim. Cosmochim. Acta* **201**, 65–82.

MacPherson G. J., Defouilloy C. and Kita N. T. (2018) High-precision Al–Mg isotopic systematics in USNM 3898 – The benchmark "ALL" for initial ^{87}Sr/^{86}Sr in the earliest Solar System. *Earth Planet. Sci. Lett.* **491**, 238–243.

Makide K., Nagashima K., Krot A. N., Huss G. R., Ciesla F. J., Hellebrand E., Gaidos E. and Yang L. (2011) Heterogeneous distribution of ^{26}Al at the birth of the solar system. *Astrophys. J. Lett.* **733**, L31–L34.

Norris T. L., Gancarz A. J., Rokop D. J. and Thomas K. W. (1983) Half-life of ^{26}Al. *J. Geophys. Res.* **88**, B331–B333.

Park C., Nagashima K., Krot A. N., Huss G. R., Davis A. M. and Bizzarro M. (2017) Calcium-aluminum-rich inclusions with fractionation and unidentified nuclear effects (FUN CAIs): II. Heterogeneities of magnesium isotopes and ^{26}Al in the early Solar System inferred from in situ high-precision magnesium-isotope measurements. *Geochim. Cosmochim. Acta* **201**, 6–24.

Schiller M., Connelly J. N., Glad A. C., Mikouchi T. and Bizzarro M. (2015) Early accretion of protoplanets inferred from a reduced inner solar system ^{26}Al inventory. *Earth Planet. Sci. Lett.* **420**, 45–54.

Sheng Y. J., Wasserburg G. J. and Hutcheon I. D. (1992) Self-diffusion of magnesium in spinel and in equilibrium melts: Constraints on flash heating of silicates. *Geochim. Cosmochim. Acta* **56**, 2535–2546.

Ushikubo T., Tenner T. J., Hiyagon H. and Kita N. T. (2017) A long duration of the ^{16}O-rich reservoir in the solar nebula, as recorded in fine-grained refractory inclusions from the least metamorphosed carbonaceous chondrites. *Geochim. Cosmochim. Acta* **201**, 103–122.

Wark D. A. and Lovering J. F. (1977) Marker events in the early solar system: evidence from rims on Ca-Al-rich inclusions in carbonaceous chondrites. In *Proceedings, 8th Lunar and Planetary Science Conference*, pp. 95–112.

Wark D. A. and Lovering J. F. (1982) The nature and origin of type B1 and B2 Ca-Al-rich inclusions in the Allende meteorite. *Geochim. Cosmochim. Acta* **46**, 2581–2594.

Wark D. A. (1987) Plagioclase-rich inclusions in carbonaceous chondrite meteorites: liquid condensates? *Geochim. Cosmochim. Acta* **51**, 221–242.

Wasserburg G. J., Lee T. and Papanastassiou D. A. (1977) Correlated O and Mg isotopic anomalies in Allende inclusions: II. Magnesium. *Geophys. Res. Lett.* **4**, 299–302.

Wasserburg G. J., Wimpenny J. and Yin Q.-Z. (2012) Mg isotopic heterogeneity, Al-Mg isochrons, and canonical ^{26}Al/^{27}Al in the early solar system. *Meteorit. Planet. Sci.* **47**, 1980–1997.

Yurimoto H., Ito M. and Nagasawa H. (1998) Oxygen isotope exchange between refractory inclusion in Allende and solar nebula gas. *Science* **282**, 1874–1877.

Yurimoto H., Koike O., Nagahara H., Morioka M. and Nagasawa H. (2000) Heterogeneous distribution of Mg isotopes in anorthite single crystal from Type-B CAIs in Allende meteorite. (abstract #1593). *31st Lunar and Planetary Science Conference*.

Yurimoto H., Krot N. K., Choi B., Aléon J., Kunihiro T. and Brearley A. J. (2008) Oxygen isotopes in chondritic components. In *Oxygen in the Solar System. Reviews in Mineralogy and Geochemistry*, vol. 68 (ed. G. J. MacPherson). Mineralogical Society of America, Washington, D.C., pp. 141–186.

Associate editor: Anders Meibom